

Improvements in calibration of GSO scintillators in the *Suzaku* Hard X-ray Detector

Shin'ya YAMADA¹, Kazuo MAKISHIMA¹, Kazuhiro NAKAZAWA¹, Motohide KOKUBUN²,
Madoka KAWAHARADA², Takao KITAGUCHI⁵, Shin WATANABE²,
Hiromitsu TAKAHASHI³, Hirofumi NODA¹, Hiroyuki NISHIOKA¹, Kazuyoshi HIRAGI³,
Katsuhiro HAYASHI³, Kenta NAKAJIMA¹, Makoto TASHIRO⁴, Makoto SASANO¹,
Sho NISHINO³, Shunsuke TORII¹, Soki SAKURAI¹, Tadayuki TAKAHASHI^{2,1},
Tsunefumi MIZUNO³, Teruaki ENOTO⁶, Takayuki YUASA¹, Takaaki TANAKA⁷,
Tomomi KOUZU⁴, Toshio NAKANO¹, Yasushi FUKAZAWA³, Yukikatsu TERADA⁴,
Yasunobu UCHIYAMA⁷, Wataru IWAKIRI⁴, and the HXD team

¹ *Department of Physics, University of Tokyo*

7-3-1, Hongo, Bunkyo-ku, Tokyo, 113-0033, Japan

² *Department of High Energy Astrophysics, Institute of Space and Astronomical Science (ISAS),
Japan Aerospace Exploration Agency (JAXA), 3-1-1 Yoshinodai, Sagamihara, Kanagawa 229-8510*

³ *Department of Physics, Hiroshima University,*

1-3-1 Kagamiyama, Higashi-Hiroshima, Hiroshima 739-8526

⁴ *Department of Physics, Saitama University,*

Shimo-Okubo, Sakura-ku, Saitama-shi, Saitama 338-8570

⁵ *California Institute of Technology, 1200 East California Blvd., Pasadena CA 91125, USA*

⁶ *KIPAC/Stanford University 2575 Sand Hill Road, Menlo Park, CA 94025, USA*

⁷ *Stanford Linear Accelerator Center, 2575 Sand Hill Road, Menlo Park, CA 94025, USA*

yamada@junophys.s.u-tokyo.ac.jp

(Received 2010 November 14; accepted 2011 May 23)

Abstract

Improvements of in-orbit calibration of GSO scintillators in the Hard X-ray Detector on board *Suzaku* are reported. To resolve an apparent change of the energy scale of GSO which appeared across the launch for unknown reasons, consistent and thorough re-analyses of both pre-launch and in-orbit data have been performed. With laboratory experiments using spare hardware, the pulse height offset, corresponding to zero energy input, was found to change by $\sim 0.5\%$ of the full analog voltage scale, depending on the power supply. Furthermore, by carefully calculating all the light outputs of secondaries from activation lines used in the in-orbit gain determination, their energy deposits in GSO were found to be effectively lower, by several percent, than their nominal energies. Taking both these effects into account, the in-orbit data agrees with the on-ground measurements within $\sim 5\%$, without employing the artificial correction introduced in the previous work (Kokubun et al. 2007). With this knowledge, we updated the data processing, the response, and the auxiliary files of GSO, and reproduced the HXD-PIN and HXD-GSO spectra of the Crab Nebula over 12–300 keV by a broken powerlaw with a break energy of ~ 110 keV.

Key words: instrumentation: detectors — X-rays: general — X-rays: individual (Crab Nebula)

1. Introduction

The fifth Japanese X-ray satellite *Suzaku* (Mitsuda et al. 2007), carries the X-ray Imaging Spectrometer (XIS; Koyama et al. 2007) located at the foci of the X-ray Telescope (XRT Serlemitsos et al. 2006) and a non-imaging hard X-ray instrument, the Hard X-ray Detector (HXD). The HXD covers a hard X-ray energy range of 10–600 keV, utilizing Si-PIN diodes (hereafter HXD-PIN), and gadolinium silicate scintillators ($\text{Gd}_2\text{SiO}_5\text{:Ce}$, hereafter HXD-GSO) which are placed behind HXD-PIN. The detailed design of the HXD is summarized in Takahashi et al. (2007) (hereafter Paper I), followed by a report on its in-orbit performance (Kokubun et al. 2007; hereafter Paper II) and that of the timing property (Terada et al.

2008).

Prior to the launch on 2005 July 10, the performance of the HXD was tested and calibrated at every stage of its integration, and also after the instrument was mounted on the spacecraft. In addition to these pre-launch experiments, several Monte-Carlo simulations were performed, to better understand the HXD performance (including its background) expected in near-Earth radiation environments (Terada et al. 2005; Paper I). We have also calibrated the HXD performance extensively after the launch (Paper II), and compared all properties that can be obtained in-orbit with the results of the ground measurements. As a result, we have successfully verified that the HXD performs in-orbit generally as expected (Paper II), and reconfirmed most of the results of the pre-launch cal-

ibration.

In spite of these successful in-orbit calibration efforts, we are still left with a few unsolved issues of the HXD performance. One of them is an apparent change in the energy scale (relation between the incident X-ray energy and detector pulse height) of HXD-GSO. We found this issue when we observed the X-ray pulsar A0535+26, which exhibits an absorption line at ~ 50 keV (Terada et al. 2006); this spectral feature appeared at discrepant energies in the HXD-PIN and HXD-GSO spectra that were produced based on the nominal pre-launch calibration (see subsection 2.3). Since the energy scale of HXD-PIN was kept unchanged across the launch (figure 5 of Paper II), we tentatively concluded that the energy scale of HXD-GSO changed for some unspecified reasons, and hence added an artificial non-linearity to the GSO energy scale (figure 12 of Paper II) as a temporary solution.

The aim of the present paper is to more fundamentally solve this issue, by revisiting the pre-launch and in-orbit calibrations, and conduct some laboratory experiments using spare hardware. Section 2 is used to review the way of conversion from energy to pulse height, and to present the investigation strategy. In section 3, we study the spare hardware performance, followed in section 4 by a detailed comparison between the on-ground and in-orbit data, and construction of a revised energy scale. We present in section 5 how well our new solution worked on actual observation data, and summarized these works in section 6.

2. The HXD Experiment

We start with a brief summary of the HXD in section 2.1, and then the procedure of the energy scale in section 2.2. In section 2.3, the in-orbit calibration that had been performed until Paper II are summarized. Other unsolved issues are introduced in section 2.4. We present our methods to tackle the problem in section 2.5.

2.1. The hardware configuration

As detailed in Paper I, the HXD consists of three major components: a sensor part (HXD-S), an analog electronics part (HXD-AE), and a digital electronics system (HXD-DE). HXD-S has a compound-eye configuration, made of 4×4 well-type phoswich detectors (“Well-counter units”), surrounded by 20 thick active shields (“Anti-counter units”). A Well-counter unit consists of 4 Si-PIN diodes and 4 GSO scintillators, all placed inside a deep well of active shields formed by BGO scintillators. Each unit outputs 4 Si-PIN signals and one GSO signal, after scintillation light from the 4 GSOs is detected by a single photomultiplier tube (PMT) which also detects light from the BGO shield. All signals of 36 PMTs (16 Well-counter and 20 Anti-counter units) and 64 PIN diodes are fed in parallel into HXD-AE, where they are amplified, pulse-shape discriminated, and analog-to-digital converted. The digitized signals are further processed by HXD-DE using an on board CPU.

The present paper pertains to the GSO scintillators (HXD-GSO) of the Well-counter units, as well as to HXD-

AE, but not to HXD-DE. It does not deal with the Anti-counter units in HXD-S, either.

2.2. Energy to pulse-height conversion

Let us briefly review the flow of converting the pulse-height into energy as described in Paper II. In any radiation detector that detects individual particles (including photons) as electronic pulses, the energy scale is critically important to its performance. Its determination is significantly more difficult in hard X-rays, than in energies below ~ 25 keV where we can utilize various celestial/instrumental atomic lines and built-in calibration radio-isotopes. In the particular case of HXD-GSO, the energy E of a detected photon is converted into pulse height, or more properly, “pulse invariant”, P , through a process shown in figure 1. A photon with an energy of E , totally absorbed in a GSO scintillator, creates a photoelectron which immediately produces many secondary electrons. These electrons deposit their energies in the scintillator, creating optical photons of a total number L (which is called light yield). The photons are (partially) detected by a PMT (Hamamatsu R6231), to get multiplied into an electronic pulse with charge Q . This charge is converted into a voltage pulse V in a charge sensitive amplifier (CSA). The process up to this stage takes place in HXD-S. The pulse sent to HXD-AE is further amplified and shaped therein by a shaper, then peak-held in an application-specific integration circuit, and finally digitized by a 12-bit analog-to-digital converter. Thus, a photon energy up to $E \sim 600$ keV is converted into a 12-bit pulse height, H .

Although the pulse height H is approximately proportional to E with a constant coefficient of proportionality, there are at least following effects that can cause deviations and/or time variations in the E vs. H proportionality.

- (1) Non-linearity in the GSO light yield (Uchiyama et al. 2001).
- (2) The overall coefficient of proportionality, or “gain”, denoted G .
- (3) Differential and integrated non-linearity in the amplification chain in HXD-AE (Kitaguchi et al. 2006).
- (4) The offset signal in analog electronics, or the “pedestal” defined in Paper II, denoted H_o in this paper. This means a value of H when no signal is present in GSO ($E = L = Q = 0$).

The effect (2) is further decomposed into the GSO light yield, the PMT gain, the CSA capacitance, and electronics settings. As detailed in Paper II, the GSO light yield depends on the temperature, while the PMT gain varies by $\sim 10\%$ in a complex way, depending on the temperature, time since the launch, and time after passing through South Atlantic Anomaly, wherein the PMT high voltage is turned off for ~ 20 minutes or less. Therefore, this coefficient, G , must be determined from moment to moment. In contrast, the effects (1), (3), and (4) are considered approximately constant with time, and were determined in the ground measurements; therefore, we can apply these

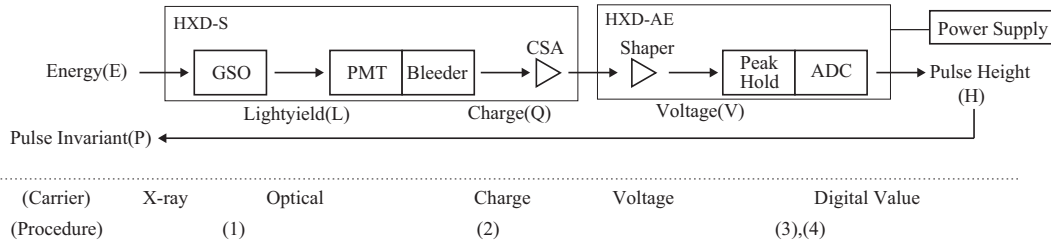


Fig. 1. A functional diagram of the energy scale of GSO. The signal carrier at each stage and the corresponding steps listed in subsection 2.2 are summarized at the bottom.

results to the in-orbit data unless something in hardware did change.

Given the knowledge on the effects (1)-(4), we can convert the pulse height H of each event into a quantity called pulse invariant (P) through the reverse procedure of figure 1. If (1)–(4) are correct, P should coincide with E within the detection energy resolution (statistical effect) and calibration uncertainties in the energy scale (systematic effects).

2.3. In-orbit calibration until Paper II

During the initial in-orbit calibration phase of Suzaku, we applied the ground-determined (1), (3), and (4) to the actual in-orbit HXD-GSO data. As explained in section 2.2, G must be determined every ~ 50 minutes, so we used for that purpose GSO background lines at 511 keV, ~ 350 keV, and 153 keV (table. 7 of Paper II for details). At that time, the energies of these lines were considered to be well defined, because they are based on nuclear physics, and the effect of non-linearity of (1) and (3) are negligible at least in > 100 keV. Thus, by fitting these lines on the E vs. H plane with a linear function [equation (1) in Paper II], we determined the slope G and the intercept of the line with the H axis, hereafter H_i , allowing both to vary. As a typical case, the employed data points (on the E vs. H plane) and the linear function (green) for one Well Unit (W31) are shown in figure 2, which is almost the same as figure 12 in Paper II. The data points include background gamma-ray lines at 70 keV, 150 keV, 193 keV, ~ 350 keV, and 511 keV. Here H is expressed in units of ADC channels, with its maximum, 4096, corresponding to ~ 700 keV. Then, H_i has appeared at ~ -50 channels (Paper II), in contrast to $H_i \sim -10$ channels measured in the ground calibration (Paper I). This means apparent changes by $\Delta H_i = -40$ between the post- and pre-launch calibrations.

Although the non-zero value of ΔH_i suggests some changes in the GSO energy scale in energies of $\lesssim 70$ keV, there are no appropriate spectral features in the ~ 10 to ~ 70 keV range to be used for calibration. Accordingly, a celestial object named A0535+26 was utilized to calibrate the energy scale down to ~ 50 keV (Terada et al. 2006), because it is known to exhibit a cyclotron resonance absorption line as shown in black in figure 3. The feature was clearly detected by HXD-PIN at an energy of ~ 45 keV (Terada et al. 2008). However, as shown in green in figure 3 and plotted in cyan in figure 2, the same feature

was seen at about 60 keV ($H \sim 205$) in the GSO spectrum, when the detected H was converted back to P by applying (1)-(4) and extrapolating the energy scale determined over 70–511 keV (dotted green line in figure 2) to energies below 70 keV. More specifically, this procedure appears to assign too high a value of E for a given H of HXD-GSO, or conversely, to underestimate H for GSO events with $E \sim 45$ keV. This could be regarded as being caused by the change of $\Delta H_i \simeq -40$ mentioned above.

The observation of A0525+26 thus revealed a $\sim 20\%$ discrepancy between the energy scales of HXD-PIN and HXD-GSO at lower energies. However, the energy calibration of HXD-PIN is more reliable than that of GSO, because its energy scale is mostly determined by the preamplifier capacitance. Furthermore, an instrumental peak due to escaping Gd-K line photons, expected at 43 keV, correctly appeared at 43 ± 1 keV in the in-orbit background spectra of HXD-PIN. Therefore, we had to conclude that the problem is in HXD-GSO, rather than in HXD-PIN.

In order to reconfirm the inference derived from the A0535+26 data, Paper II utilized pedestal information H_o on the PMT signal, i.e., the value of H when the energy deposit E approaches 0. This H_o can be obtained not only during the pre-launch tests, but also from the in-orbit data, by referring to values of H of those events which were triggered by the PIN diodes in the same Well-counter unit: even for such events, the PMT pulse heights are latched, and sent out to telemetry, for later use in the background rejection. In fact, this gives $H_o + \delta$, where δ is contribution from noise in the PMT signal and can be estimated to be less than ~ 1 keV (~ 4 ch). The value of H_o derived in this way is given in figure 2b as a data point at $E \sim 0$ and $H_o \sim 80$. Thus, the problem uncovered by the A0535+26 data was reconfirmed. This effect exceeds what can be explained by (1) and (3).

To temporarily solve this apparent discrepancy in the energy scale of GSO below ~ 70 keV, an additional non-linearity (the third term of equation 2 in Paper II) has been artificially introduced. As a result, the GSO spectrum of A0535+26 moved to lower energies (blue spectrum in figure 3), and the cyclotron absorption-line energy measured with HXD-GSO became consistent with that of HXD-PIN. Although the blue spectrum in figure 3 still shows a somewhat higher absorption-line energy than the black one, the difference can be explained away by a poorer energy resolution of HXD-GSO than HXD-PIN,

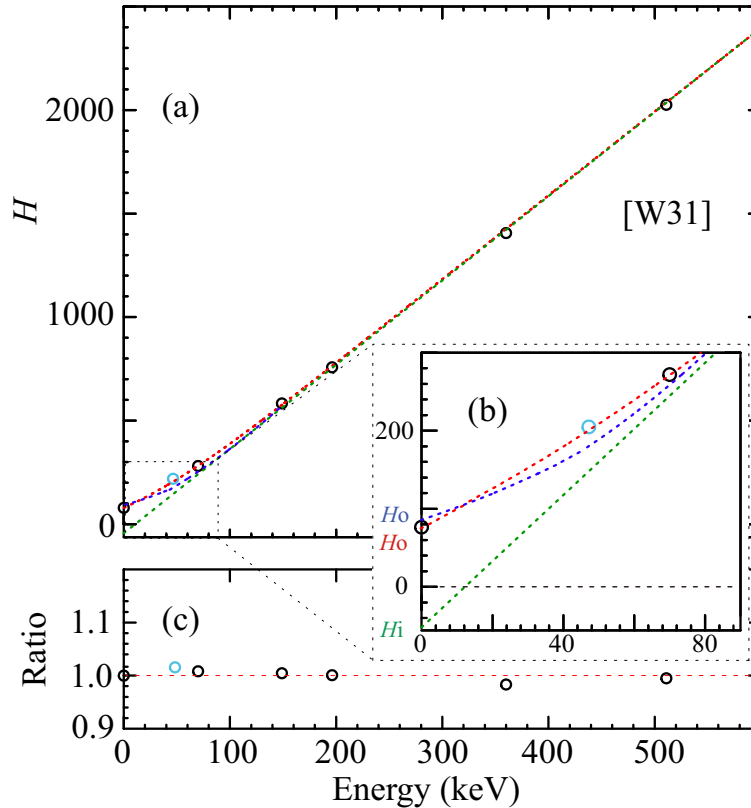


Fig. 2. (a) Initial in-orbit calibration of the GSO energy scale. Abscissa is the input energy E , while ordinate is the pulse height H . In addition to several background lines, the cyclotron line of A0535+26 at ~ 50 keV (cyan), and the “pedestal” information at 0 keV are also shown. The green line represents the linear relation derived by fitting three background lines, and the red one is the final energy scale of GSO derived in the present study. The blue curve is the tentative solution introduced in Paper II by invoking an artificial bending. (b) An expanded view of the lower energy range of (a). (c) The ratio of the red line to the data points.

coupled with a steeply declining continuum. In figure 3, the entire spectra are divided by the Crab Nebula spectrum which behaves as $\propto E^{-2.1}$.

2.4. Other differences between on ground and in-orbit data

In addition to the above issue of the GSO energy scale, the in-orbit data exhibited some other anomalies which cannot be fully explained by the pre-launch calibration. When Paper II was compiled, it was not clear whether either or both of these two unexpected effects comes from the same origin as the GSO energy scale problem. These issues are discussed in section 5.

One is the performance of pulse-shape discrimination, which is applied to the PMT signal in HXD-AE to distinguish GSO and BGO events (see figure 15 in Paper II). As described later in subsection 5.1, width of the GSO branch on so-called slow-fast diagram, appears to have changed across the launch. The other is that the current response matrix for GSO is overpredicting the spectrum by 10% in energies below 100 keV, as evidenced by a Crab spectrum of GSO (figure 18 in Paper II). For a temporary settlement, an artificial ancillary response file has been provided.

2.5. Working hypotheses and verification methods

Although the unexpected change in the GSO energy scale below ~ 70 keV is at present absorbed by the artificial correction factor, this is a temporary and empirical solution. More fundamentally, we need to understand the cause of the change, and if necessary, update the GSO energy scale.

In the following, we conduct two approaches towards the above objectives. One of them is to examine the HXD hardware performance for any launch-related changes. This is carried out in section 3, partially incorporating laboratory experiments using scintillators, phototubes, preamplifiers, and analog electronics that are all (nearly) equivalent to the actual flight-model HXD.

The other approach to our goal is to examine the process of energy calibration, searching for any inaccuracy or inconsistency between the pre- and post-launch calibrations. In section 4, we therefore re-analyze the in-orbit GSO data, as well as the pre-launch calibration data which were taken by irradiating various calibration isotopes to the HXD. Through a consistent data analysis, we try to understand more accurately how the energy scale had changed across the launch.

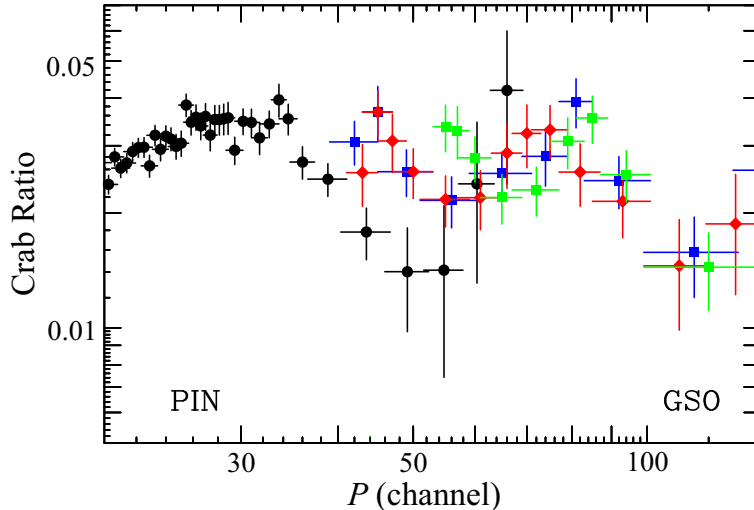


Fig. 3. Crab ratio spectra of A0535+26, as a function of the pulse height invariant, P . The one obtained with HXD-PIN is shown in black. The green one is obtained with HXD-GSO with the initial energy scale, while the blue one is after including the artificial correction given in figure 2 (blue curve) and Paper II. The red one is created by using the energy scale obtained in this paper.

3. Examination of the hardware performance

3.1. Possible changes in the HXD hardware

The first of the two approaches mentioned in section 2.5 is based on a concern that the present issue can be a result of some changes in the HXD hardware performance, including its scintillators, PMTs, CSAs, bleeders, and electronics; in other words, anywhere in the diagram of figure 1. This is further subdivided into the following three general possibilities. One is that the launch stress caused some irreversible changes (including damages) to the HXD hardware. Another is that frequent large-amplitude scintillation pulses, produced by charged particles in the space environment, brought about some differences in the low-energy response. The other is that the spacecraft power supply, which is known to be less stable than those used in laboratory, may have caused some changes in the electronics response to low-pulse-height signals.

We found that the former two possibilities do not affect the energy scale, so that we summarized them in Appendix 1 and 2, respectively. In the next subsection, we examine the third possibilities that actually affected the energy scale of the GSO.

3.2. Effects of the power supply

A clear difference in the hardware environment between the ground and in-orbit measurements is the power supply. Our ground calibration was performed using general-purpose power supplies (+12 V, -12 V, +5 V analog, and +5 digital), which are more stable than the flight one. This could affect the HXD-AE performance, particularly at low pulse heights. Although HXD-AE does not have its own calibrators, the raw pulse height accumulated during no signal inputs in GSO, i.e., pedestal (H_o in figure 2), can be used for this purpose. The values of the pedestal have been compared among three data sets: (1) the on-ground calibration data acquired in June 2004, using a labora-

tory power supply, where the HXD was not yet mounted on the spacecraft; (2) the on-ground data taken in 2004 August with the HXD mounted on the spacecraft, and driven by the flight power supply; and (3) in-orbit data acquired from a black sky in June 2007 during a period when the PMT high voltage was temporary turned off to avoid over/under shoot caused by cosmic ray signals. As explained in section 2.3, the pedestal signal, H_o , was obtained by selecting cosmic rays or background events triggered uniquely by HXD-PIN.

Figure 4 shows histograms of H_o for the 16 Well-counter units. Thus, they show $H_o \sim 81$ channels when HXD-AE was driven by laboratory power supplies. In contrast, they exhibited $H_o \sim 73$ channels when the flight power supply was used, both before or after the launch. The change by $\Delta H_o \sim -8$ can be attributed to the difference in the power supplies, because everything else was the same. However, as illustrated in figure 2, the effect, at most $\sim 4\%$ for the 50 keV signals (equivalent to $H \sim 200$), is not large enough to account for the $\sim 20\%$ change of energy scale at ~ 50 keV (section 2.3); some other effects are needed.

4. A Unified Analysis of Ground and In-Orbit data sets

We start with examination of ground calibration data in section 4.1, and then, employing newly introduced “ Q vs. H ” plot in section 4.2, compare the ground data to in-orbit data in section 4.3. The examination on light yield and reanalysis of in-orbit data are summarized in section 4.4 and 4.5.

4.1. Summary of ground calibrations

Since we have found that the change in hardware cannot explain the change of the E vs. H relation, we then proceed to the second approach introduced in section 2.5, and try to review our calibration processes, starting with

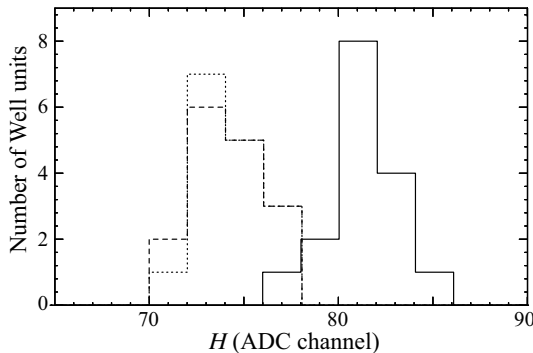


Fig. 4. Histograms of the number of Well-counter units as a function of H_o for the three conditions; the solid, dotted, and dashed lines indicate pre-launch data taken in laboratory, those obtained on the spacecraft, and in-orbit data, respectively.

that on ground data.

Although an inorganic scintillator has a roughly constant L (subsection 2.2) of its own, the E vs. L proportionality is in many cases only approximate, and needs detailed calibration. Such measurements of GSO used in the HXD were performed by Kitaguchi et al. (2005), irradiating gamma-rays from various radio-isotopes.

Q vs. H calibration on ground in June 2004 were performed by Kawaharada et al. (2004), by inputting electronic test pulses of various pulse heights simultaneously to HXD-AE and a laboratory MCA (the same as used in section 3.2). When the latter was used as an ideal reference, HXD-AE was found to have a good Q vs. H proportionality at $H \gtrsim 200$ ($\gtrsim 50$ keV), with slight non-linearity below $H \sim 200$.

In addition to these basic measurements, end-to-end pre-launch calibrations were performed by irradiating gamma-ray isotopes to GSO from outside and processing the signals with HXD-AE. The acquired data are of high importance, because they can be compared directly with the in-orbit data.

Here, we have analyzed such pre-launch GSO calibration data, taken by Kawaharada et al. (2004) in June 2004 under the same condition as (1) in section 3.2 (i.e., using a laboratory power supply). Of the 16 Well-counter units, we use the W31 unit for simplicity, because the HXD-AE performance is almost the same among the 16 channels (Paper I). Thus, we can use the results to compare them with the in-orbit data.

4.2. Introduction of “ Q vs H ” plots

When comparing different sets of calibration data, we usually create from each data set an “ E vs. H plot”, wherein the measured pulse heights H are plotted against the known photon energies E . A comparison between a pair of E vs. H plots requires their appropriate corrections for the difference in the overall gain G , which varies depending mostly on the PMT gain. This is usually done by renormalizing the H values from one of the plots to a certain constant factor, so that these plots become close

to each other. This renormalization procedure is correct if, for example, the E vs. H relation deviates from an exact proportionality mainly due to the GSO non-linearity between E and L ; however, it is not if the deviation is dominated by electronics effects and hence is dependent on H , not E or L . More generally, an E vs. H relation may be approximated as $H = GE + H_o$ at small values of E , and it is not trivial how to deal with H_o when renormalizing; should we calculate as $H \rightarrow \beta(GE + H_o)$, or $\beta GE + H_o$, or in other ways (where β is the renormalization factor)?

To avoid the above problem, we have introduced a new concept of “ Q vs. H ” plot (Yamada 2008), where Q means the charge (figure 1) coming out of the PMT. The new plot can be obtained from an ordinary E vs. H plot in the following manner. First, the energy E (assumed to be known) of each data point is converted into the light yield L through the knowledge on the GSO light yield (Kitaguchi 2006), or E vs. L relation, which is implicitly assumed to be rather stable across the launch. Then, the charge Q is defined as a quantity proportional to L , without any zero-point offsets; this is justified by the general property of PMTs. The constant of proportionality between Q and L is determined so that the value of Q becomes identical to that of E (in units of keV) at the most reliable high-energy data point. Thus, Q is defined to take roughly the same values as E , and is considered to be free from the GSO non-linearity and the PMT gain changes. The most time-variable factor, namely G , is renormalized at this stage. In other words, we compare different calibration plots by adjusting their energy axes, rather than by stretching/compressing their pulse-height axes. This procedure implicitly assumes little changes in the HXD-AE performance.

4.3. Comparison between the ground and in-orbit calibration results

Figure 5 is the “ Q vs. H ” plot constructed via the above procedure from the ground calibration data (green) and in-orbit data (red). The gain of the ground data were re-adjusted (along the horizontal axis) so that they match the in-orbit ones. To guide the eyes, a proportionality line pointing from the origin to the data corresponding to 511 keV is superposed, and ratios of the data to this line are shown in figure 5b. In the lower-ADC channel ($\lesssim 200$ ch) region, the ground calibration data exhibit $\sim 10\%$ deviation above the linear function. As described in subsection 3.3, this offset is attributable to the non-ideal Q vs. H properties of HXD-AE (Kawaharada et al. 2004). Actually, when the on-ground data points are corrected for this effect, the deviation from the proportionality line diminishes to less than 4%; this means that the energy scale of GSO for the on-ground data consists of all known factors.

Figure 5b reveals two systematic differences between the pre-launch and in-orbit calibration data sets. One is that the in-orbit data points fall systematically below the line of proportionality, in energies from 60 to 400 keV: this effect is not observed in the ground calibration data.

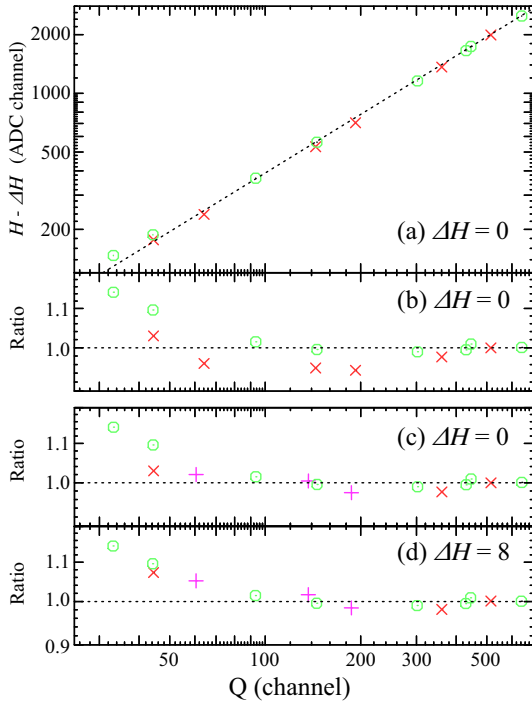


Fig. 5. A Q vs. H plot. Abscissa is Q , while ordinate is H but ΔH has been subtracted if needed. The gain is re-adjusted so that the on-ground data match the in-orbit ones. The errors are smaller than the size of plotting symbols. (a) The green circles are the pre-launch data, while the red crosses represent the in-orbit data points. The dotted black line is a proportionality line connecting the origin to the 511 keV point. (b) Ratios of the in-orbit and pre-launch data to the common line of proportionality defined in panel a. (c) The same as (b), but the value of Q of the in-orbit lines at 70, 150, and 196 keV (pink crosses) are re-calculated (section 4.4). (d) The same as (c), but H of the in-orbit data are lowered by $\Delta H = 8$ ch considering the results of section 3.3

The other is that the in-orbit data points in the pulse-height range below $H \sim 250$ ch exhibit much milder excess above the proportionality line, than the ground data points. Thus, the energy scale appears to have really changed across the launch. However, it is apparently inconsistent with the result that in-orbit data exhibit *larger* excess toward lower pulse heights than the pre-launch data (cf. figure 2; figure 12 in Paper II).

As explained in section 2.2 and figure 2, the first approximation of energy scale was derived by connecting the 150 keV, 350 keV, and 511 keV data points with a linear (not proportional) function, in which the slope and offset are both allowed to change. This linear function, with an intercept of $H_i = -50$ (figure 2), has a steeper slope than the line of proportionality (with $H_i = 0$) employed in figure 2. If this steeper line is instead used in figure 5, the in-orbit data in panel (b) would exhibit much larger positive residuals in $H \lesssim 200$, while the intermediate-energy data points would fall right on the line, thus reproducing the behavior seen in figure 2. Considering the result in section 3 that the hardware performance has not changed as much, it is therefore more reasonable to consider that the signifi-

cant low-energy excess observed in figure 2 and Paper II is caused artificially because we started from an inappropriate linear function with a steeper slope (and hence with a large negative H_i). If this is true, the next question is what has caused the line, connecting 150, 350, and 511 keV points, to have a wrong slope. Let us consider how the energies of these activation/annihilation lines seen in the in-orbit background spectra are measured with HXD-GSO.

4.4. Re-examination of Light yield from activation lines

Among the instrumental background lines used in the in-orbit energy calibration of HXD-GSO, the 511 keV electron-positron annihilation line is based on a simple elementary process, with its photo-peak created by absorption of a single mono-energetic gamma-ray line. In contrast, as described in Table 7 in Paper II, the activation lines at 70 keV, 150 keV, and 196 keV are statistical mixtures of various radiation components, including nuclear transition gamma-rays, fluorescent X-rays, Auger electrons, and internal conversion electrons. This raises a suspect that the values of L for the 150 keV and 350 keV activation lines would differ from their nominal values.

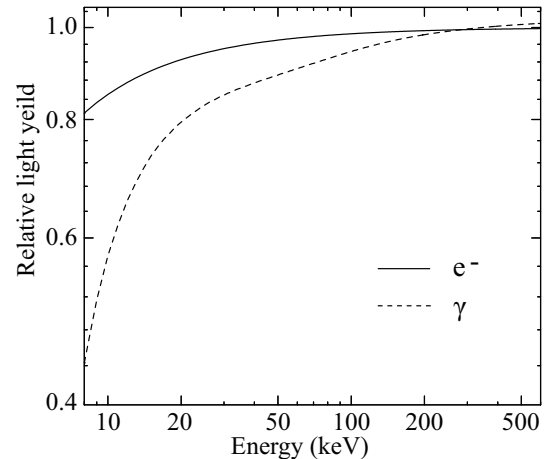


Fig. 6. Relative light yield of GSO as a function of energy. The solid curve is for incident electrons (Uchiyama et al. 2002), and the dashed one for photons (Kitaguchi et al. 2005).

The values of light yield, L , from activation lines have been so far calculated by assuming that their energy is deposited in GSO by a single gamma-ray photon. However, this approximation might be over-simplified, because electrons and photons give different L in GSO and their energy deposited in GSO are not perfectly proportional to L . Figure 6 shows the light yield against energy for electrons (Uchiyama et al. 2001) and photons (Kitaguchi et al. 2006), which are both experimentally measured and normalized at 344 keV. Thus, the two curves are both considerably non-linear, and are different from each other. Therefore, even if the overall energy released by a nuclear decay is the same, the light output depends on how the total energy is split into individual components, and whether they are photons or electrons. Taking into ac-

count figure 6, we evaluate the light output for the three background lines (70 keV, 148 keV, and 196 keV).

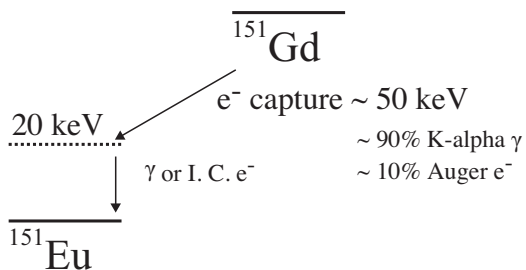


Fig. 7. The decay chain from ^{151}Gd to ^{151}Eu which produces the background peak in GSO spectra at an energy of 70 keV.

For each activation line, we analyzed the decay processes involved therein, and calculated their energy releases and branching ratios. This was done using such information as nuclear activation energies, the energies of fluorescent X-rays, the fluorescent yields, and the internal conversion coefficients. Then, we calculated light outputs for all the electrons and photons using the corresponding relative light yields in figure 6, and summed up the derived light outputs weighted by their branching ratios.

Figure 7 shows an example of the decay scheme of the 70 keV line. It begins with electron capture of ^{151}Gd into ^{151}Eu . This releases an energy of ~ 50 keV, via emission of a fluorescent X-ray photon or an Auger electron, with a branching ratio of $\sim 90\%$ and $\sim 10\%$, respectively. This leaves ^{151}Eu in an excited state with a remaining energy of 20 keV, which is released by either a photon or an electron through internal conversion. A simplified example of evaluation is as follows. When a single photon emission with an energy of 70 keV is considered, the light yield is estimated as $70 \times 0.92 = 64.4$, where 0.92 can be read from figure 6; in contrast, where a photon of 20 keV, plus a 9:1 contribution from a photon of 50 keV and an electron of 50 keV are considered, the light yield can be calculated as $20 \times 0.78 + 0.9 \times 50 \times 0.9 + 0.1 \times 50 \times 0.96 = 60.9$, which is 5.4 % lower than the single-photon value of 64.4 keV. We have calculated more precisely (Yamada 2008), and described them more in detail in Appendix 3. As a result, we have found that the light outputs of 70 keV, 148 keV, and 196 keV lines decrease by 5.7%, 5.2% and 3.0%, respectively. In other words, for example, the activation line which totally deposits 70 keV in GSO should have been regarded as a light output from a single photon with an effective energy of 65.8 keV.

4.5. Re-analysis of the In-orbit Data

When the revised output (subsection 4.4) is used, the in-orbit data points for the 70, 150, 196 keV lines move to the left in figure 5a. Then, their ratio to the proportional line have become as shown in figure 5c. Thus, the in-orbit data agrees better with the ground data. However, the ratio of the in-orbit data still shows slightly lower values over 50–400 keV than the on-ground ones.

Finally, the change of the pedestal, $\Delta H_o \sim -8$, as found in section 3.2, was considered. As a result, the low-energy in-orbit data points moved in figure 5a slightly upward along the $H - \Delta H$ axis, and their ratios, figure 5d, became in full agreement with those of the on-ground data. We hence conclude that the in-orbit energy scale of GSO is consistent with the on-ground one within an accuracy of $\sim 5\%$, and the apparent change of the in-orbit data is caused partially by the differences of HXD-AE power supplies, and more fundamentally, by the overestimation of light outputs from the activation lines employed in the in-orbit calibration. The artificial nonlinearity introduced in Paper II and mentioned in section 1 is no longer needed.

As a further confirmation, we overlaid the GSO spectra of A0535+26 in red in figure 3. The red spectrum agrees with the blue one at $P \sim 50$, which means that the energy scale of GSO agrees with that of PIN at ~ 50 keV; while the red one around $P \sim 70-200$ is slightly shifted to the left side by $\sim P$ channels \sim keV, which is caused by the recalculation of the light yield preformed in section 4.4. Thus, we have succeeded in obtaining more correct energy scale of the GSO than the previous one, without relying on the artificial correction introduced in Paper II.

5. Application of the revised energy scale of HXD-GSO

Since we have confirmed that the hardware did not change except for the slight pedestal shift, we have created a new energy scale of GSO and implemented it in a ftool `hxdpi` in HEADAS 6.9 or later. In this section, we described some after effects of this new energy scale, and apply it to the spectra of the Crab Nebula.

5.1. GSO branch width

Let us examine the issue of GSO branch width (for definition see figure 15 in Paper II). Figure 8 shows four GSO branch widths from the unit W00 (see caption for details). As shown in Paper II and mentioned in section 2.4, the in-orbit GSO branch (yellow) became wider below 100 keV than those of the ground calibration (green). This change can be explained as an effect of the artificial nonlinearity introduced previously, because the effect of nonlinearity works differently for fast and slow shaped pulse heights (unless they happen to have the same value). This causes a wider data distribution in a fast-slow diagram (cf. figure 2 in Paper II).

As shown in red in figure 8, this problem has nearly disappeared when we re-analysed the same in-orbit data using the new GSO energy scale established in section 4.5. Thus, we have confirmed that the in-orbit GSO branch width is consistent with the on-ground one and that the apparent change as explained in section 2.4 was caused by the incorrect energy scale of GSO. The revised GSO branch width is released as `ae_hxd_gsopsd_20090812.fits`, which must be used in `hxdgrade`.

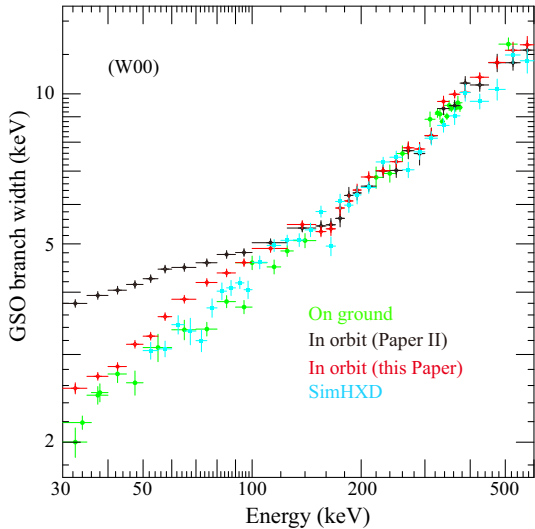


Fig. 8. The GSO branch width (Gaussian sigma) of W00 on the fast-slow diagram, shown as a function of energy. The on-ground and in-orbit data (Paper II) are shown in green and black, respectively. Cyan shows a result of Monte-Carlo simulation, and red is in-orbit data based on our new GSO energy scale.

6. Update of GSO response

The final task of our re-calibration is to update the response matrix of GSO. The calculation of the HXD energy response employs a Monte-Carlo simulator, called “simHXD” (Ozaki et al. 2006; Terada et al. 2005), based on a Geant4 framework (Sulkimo et al. 2003 and Allison et al. 2006), which has been constructed using the measured detector performance and the actual detector geometry. This simHXD assumes a bunch of input photons obeying a flat spectrum, and produces the corresponding fake HXD event data, by simulating how each input photon interacts with the HXD-PIN and/or HXD-GSO and what kind of signals it produces. Then, the simulated data are processed in the same way, using the same event selection criteria, as the actual data are analyzed. This gives an acceptance probability (and hence an effective area) for an input photon to be judged as a valid HXD-PIN or HXD-GSO event.

In the present paper, we have improved simHXD in the following three points. (1) The HXD-GSO energy scale was revised (subsection 5.1), while calculation on energy deposits were not changed. (2) The GSO branch width was updated referring to the red data in figure 8. (3) The simulator was further optimized, with respect to its usage of the GSO branch width information, and its emulation of the event selections in HXD-DE (Paper I).

In figure 8, we overlaid a result of a improved simHXD (Terada et al. 2005; Ozaki et al. 2006). The GSO branch width calculated with simHXD should be consistent with the others. In fact, they became consistent as shown in figure 8. Thus, the on-ground, in-orbit and simulated data became all consistent. The new response matrices of HXD-GSO, `ae_hxd_gsoxi(hx)nom_20100524.rsp`, has

been released in May of 2010¹.

6.1. The HXD spectra of the Crab Nebula

The Crab Nebula has been used as a standard candle in the X-ray range, because it is bright and approximately stable. Thus, it is essential to examine whether the new GSO response, created above, can explain the Crab data, without invoking the artificial correction factor which had been introduced to supplement the old response.

We analyzed two data sets of the Crab, acquired consecutively on 2005 September 15 each for 6 hours: one was obtained at the HXD nominal position from 14:00, and the other at the XIS nominal position from 19:50. The GSO data were reprocessed by `hxdpi` and `hxdgrade` with the new GSO branch width, `ae_hxd_gsopsd_20090812.fits` (section 5.1). Non X-ray backgrounds of GSO created from the same procedure, released as version 2.4, were used. We extracted HXD-PIN spectra from cleaned events, and subtracted non X-ray background (Fukazawa et al 2009) from it and used standard responses, `ae_hxd_pinxi(hx)nome1_20080129.rsp`.

The discrepancy in normalization between PIN and GSO became $\sim 20\%$, which is probably due to differences between actually observed data and simHXD on the anti-coincidence efficiency mainly triggered from Gd-K fluorescence emission lines or the depth of the depletion layers in PIN. The GSO responses around 50-60 keV is hard to calibrate due to its poorer energy resolution at these energy ranges and the photo-absorption at Gd-L shell that is not negligible at the lower energy ranges and makes the absorption process more complex than in higher energy ranges. Since these effects do not significantly affect the spectral shape over ~ 70 keV in GSO, we created the GSO auxiliary files, `ae_hxd_gsoxi(hx)nom_crab_20100526.arf`², which trims (by $\sim 20\%$) the PIN vs. GSO cross normalization, and adjust the HXD-GSO response around Gd-K edge energy (50–60 keV). The cross-normalization between HXD-PIN and HXD-GSO was fixed at 1:1, and the fitting range of HXD-PIN and HXD-GSO were 12-70 keV and 50-300 keV, respectively. The column density for photoelectric absorption was fixed at 3×10^{21} cm². The error refers to 90% significance.

We started to fit the HXD-PIN and the HXD-GSO spectra with a powerlaw. The obtained parameters are summarized in table 1, while the spectra with the best-fitted model (blue) and the ratio to the model are shown in figure 9a and b, respectively. The XIS- and HXD-nominal data were both reproduced approximately by a powerlaw, with reduced χ^2 (d.o.f) of 1.23 (132) and 1.52 (132), respectively. In both cases, the derived photon index of ~ 2.1 and the normalization of ~ 11 photons s⁻¹ cm⁻² keV⁻¹ are close to those reported previously. However, the ratio to the model, as shown in the bottom panel in figure 9a and b, falls $\sim 10\%$ below unity in energies above ~ 100 keV. This suggests that there is a mild spectral cut-

¹ http://heasarc.gsfc.nasa.gov/docs/suzaku/analysis/gso_newgain.html

² <http://www.astro.isas.ac.jp/suzaku/analysis/hxd/gsoarf2/>

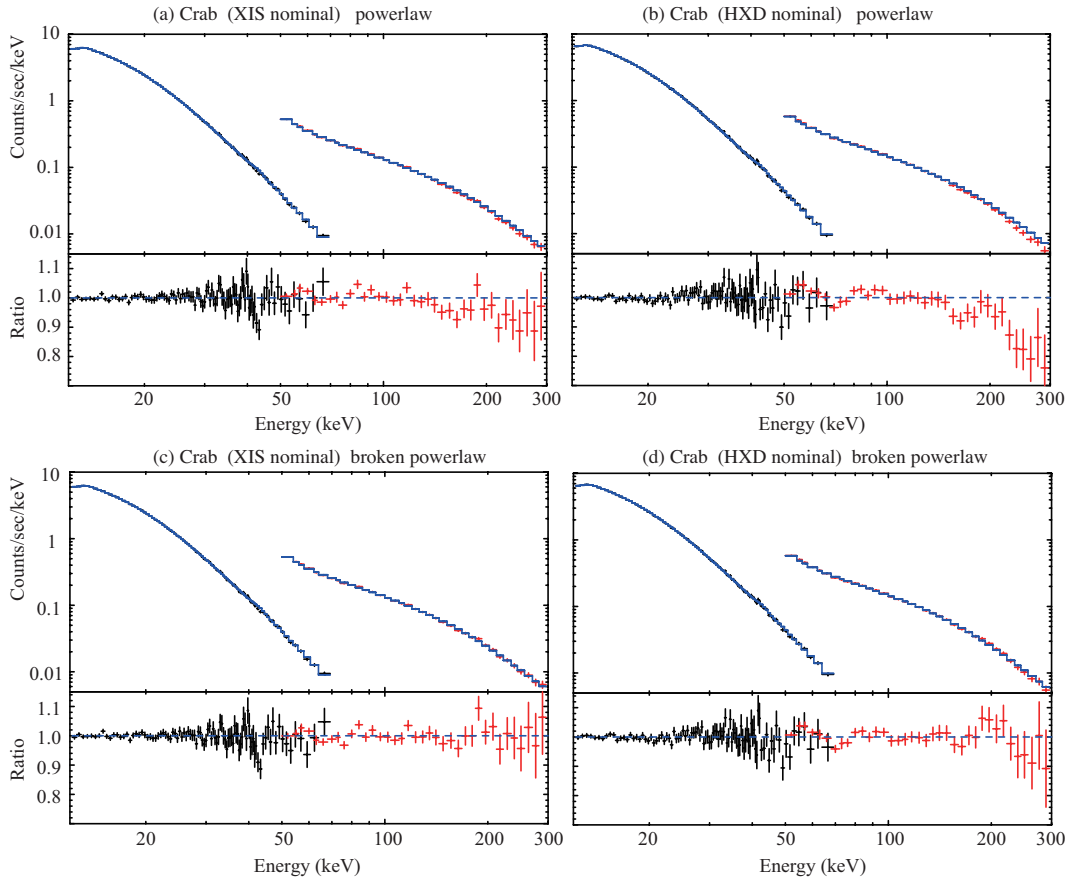


Fig. 9. The HXD-PIN and HXD-GSO spectra of the Crab Nebula, fitted simultaneously with a power-law model (top two panels labelled a and b) or a broken power-law model (two bottom panels labelled c and d).

Table 1. Fitted parameters with a single and broken powerlaw for the PIN and GSO spectra of the Crab nebula.

Target position	Photon index1 [§]	Normalization*	Photon index2 [§]	E_{break}	χ^2_{ν} (d.o.f)
XIS nominal [†]	2.109 ± 0.003	11.65 ± 0.011	-	-	1.23 (132)
HXD nominal [‡]	2.096 ± 0.003	11.14 ± 0.011	-	-	1.52 (132)
XIS nominal [†]	2.104 ± 0.004	11.47 ± 0.12	$2.21+0.06-0.04$	105 ± 20	1.04 (130)
HXD nominal [‡]	2.089 ± 0.004	10.91 ± 0.12	$2.28+0.09-0.10$	117 ± 19	1.09 (130)

Notes. The column density for the interstellar absorption is fixed at $3 \times 10^{21} \text{ cm}^{-2}$.

* Power-law normalization in a unit of photons $\text{cm}^{-2} \text{ s}^{-1} \text{ keV}^{-1}$ at 1 keV.

[†] Observation performed on 2005 September 15 19:50–September 16 02:10 (UT)

[‡] Observation performed on 2005 September 15 14:00–19:50 (UT).

[§] The photon index1 refers to $E < E_{\text{break}}$, while the photon index2 $E > E_{\text{break}}$.

^{||} The break energy of a cutoff powerlaw (keV).

off at $\gtrsim 100$ keV in the Crab spectrum, as reported in some previous studies including in particular that with INTEGRAL (Jourdain & Roques 2009).

To express the high-energy turn over, we fitted the Crab spectra with a broken powerlaw, and obtained the results as summarized in table 1 (bottom two rows) and figure 9 (panels c and d). The fits became significantly improved to reduced χ^2 (d.o.f) of 1.04 (130) and 1.09 (130), for the XIS and HXD nominal data, respectively, and the model vs. data discrepancy has been reduced to $< 10\%$. The results imply that the photon index steepens from

~ 2.1 to 2.2 – 2.3 across ~ 110 keV. These are consistent with those obtained by INTEGRAL (Jourdain & Roques 2009). Thus, we confirmed that the new response of GSO can successfully reproduce the Crab spectrum in terms of a broken powerlaw, without using the artificial correction factor needed previously.

7. Conclusion

We have performed re-calibration of the energy scale of the GSO scintillators which covers the harder energy

ranges of the Suzaku HXD. Through laboratory experiments using flight-spare hardware, we found that the pedestal of HXD-AE decreased by 8 ch when the HXD is driven by the spacecraft power supply, than the case where a more stable laboratory power supply is used. Calculating all light outputs of secondaries from activation lines revealed that the energy of calibrators, used to determine the in-flight gain of GSO, was previously overestimated by several percent. Taking both effects into account, the in-orbit data have been confirmed to be consistent with the pre-launch calibration.

When the GSO energy scale was thus revised, the in-orbit GSO branch width became also consistent with the ground one. Taking into account the energy scale thus updated, as well as the GSO branch width, the response matrixes have been created. Then, the Crab Nebula spectra of HXD-PIN and HXD-GSO, over 12–300 keV, has been expressed by a broken powerlaw with a break energy of ~ 110 keV and a photon index of ~ 2.1 below this energy.

As a result of these works, major issues with the in-orbit calibration of HXD-GSO have been successfully solved.

The authors would like to express their thanks to all who have contributed to the design, development, operation, and the calibration of the HXD experiment, and all of the Suzaku supporters. The present work was supported by Grant-in-Aid for JSPS Fellows.

Appendix 1. Irreversible Changes in the HXD Hardware

The heavy mechanical stress during the launch can produce cracks in the GSO crystals, or degrade their optical contact to the PMT entrance window. However, the energy resolution of GSO, measured after the launch using activation lines, agreed very well with that measured on ground (Paper II). Therefore, the response of the GSO crystals is unlikely to have changed significantly.

The PMTs are another critical item subject to the launch vibration. Since the launch, the PMTs have been working normally, with gain changes by $\sim 0.5\%$ and $\sim 20\%$ on short (\sim hours) and long (\sim month) time scales, respectively. Then, these gain changes may have slightly affected the PMT linearity, because the PMT bleeders use non-linear electronic parts, such as clump diodes and Zener diodes (Paper I). However, the effects of these non-linear components would appear in the highest energy range under large signals caused by cosmic rays, than in the lower energy range as we observed. Therefore, the PMT performance is considered to have remained essentially unchanged.

Electronics parts in the CSA and HXD-AE could in principle be affected by the launch stress. However, it is highly unlikely that the 16 CSAs and 16 amplification chains, which individually process signals from the 16 Well-counter units, were damaged in the same manner. Considering these, we conclude that any conceivable launch-related irreversible hardware change cannot

explain away the present issue of the GSO energy-scale change.

Appendix 2. Effects of Large Signals in the Space Environment

The HXD is exposed in-orbit to a high flux of cosmic rays, so that the PMTs receive frequent large-amplitude signals. This could affect detailed PMT responses, because their bleeders employ non-linear components as mentioned in the previous subsection. Furthermore, the response of HXD-AE may change when frequent large signals are present. The effects of large signals on PMTs and HXD-AE were studied on ground, by irradiating several isotopes to GSO, and optical pulses to the PMT at the same time (Tanihata 1998; Kawaharada 2002). According to the results, any non-linear effect did not appear in energy ranges above ~ 80 keV. However, the lower energy range has remained yet to be examined.

To study effects of large signals on low-energy events, we performed laboratory experiments using a GSO scintillator, a PMT with bleeder, a CSA, and HXD-AE, which are all the flight spares or flight equivalent components. The flight-spare GSO is of the same size, made by the same process, and its energy resolution is several percent worse than those used in the flight hardware. In-orbit, a Well-counter unit experiences a typical upper-discriminator (UD) hit rate of ~ 100 Hz (Paper II), which are mostly caused by primary cosmic rays passing through its BGO shields, since the UD threshold is set at ~ 1 MeV. Note that a typical minimum-ionizing proton with an energy of ~ 1 GeV deposits an energy of ~ 80 MeV, when it passes through the BGO bottom part (with a density of 7 g cm^{-3}) for a path length of ~ 6 cm.

Besides the GSO scintillator attached to the PMT, we placed a light-emitting diode (LED) therein, and made it flash by a pulse generator to simulate the cosmic-ray signals. The LED pulses were adjusted to have a decay time of 500 ns, and an energy deposit per pulse of 200 MeV BGO equivalent (or 50 MeV GSO equivalent) with a repetition rate of 100 Hz (\approx the UD hit rate). This value is about twice larger than an estimated energy deposit, ~ 80 keV, just to exaggerate possible effects. Then, the PMT was operated at 900 V, and the output (last dynode) signal was amplified by the CSA at a time constant of 0.5 μs . The experimental setup is shown in figure 10.

To confirm the performance from GSO to CSA, a commercial multi-channel analyzer (Amptek MCA 8000A) was used as an ideal ADC, which is known to be linear to within 1 %. To test the CSA itself, we input test pulses, created by a random pulse generator at a voltage of 5 V (equivalent to ~ 662 keV signals), into the CSA and measure its output using the MCA. To avoid the effects of overshoot or undershoot when a large signal (LED signal) comes into the PMT, the PMT anode signal was used to veto data acquisition in the MCA via a gate generator. As a result, the ADC channels of the test pulses were not affected by the LED signals by more than 1%. The result means that the CSA itself does not change under large

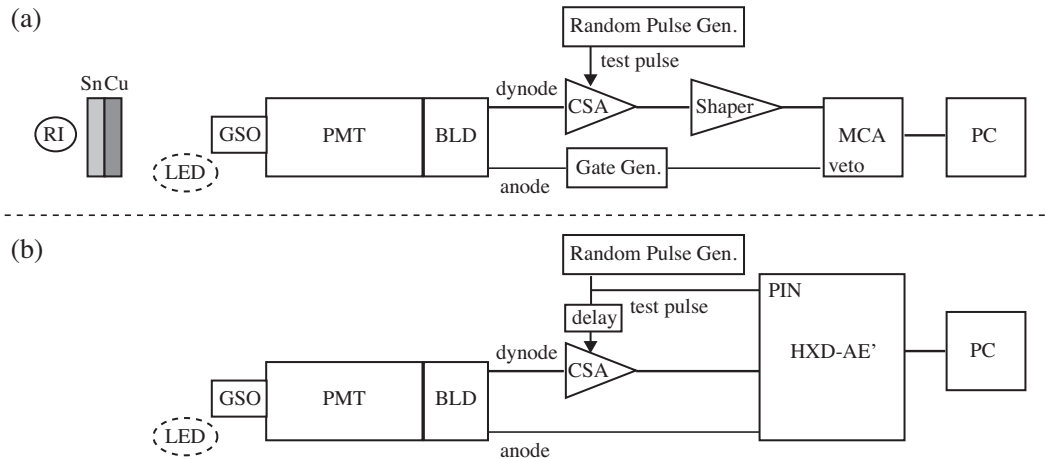


Fig. 10. The experiment setups to test the hardware behavior under large signals. The setup in (a) is used to test the response from GSO to CSA, where that in (b) to test HXD-AE.

signals.

We then proceed to the test from GSO to PMT, using the same setup, by irradiating ^{152}Eu and ^{109}Cd simultaneously to the GSO scintillator. We placed Sn and Cu plates of 5 mm thickness in front of ^{152}Eu , as shown in gray boxes in figure 10, to stop lower energy ($\lesssim 100$ keV) events. This allowed us to utilize 122 keV and 344 keV lines from ^{152}Eu , and 22 keV line from ^{109}Cd to determine the gain and non-linearity of GSO. Consequently, the GSO spectrum remained unchanged under the LED irradiation within $< 1\%$. We have thus confirmed that the performance from GSO to CSA, or before HXD-AE, does not change under large signals

To test the HXD-AE performance under large signals, a fight-equivalent HXD-AE system (hereafter HXD-AE') was used, under the setup shown in figure 10b. We put simultaneously into the CSA both the LED signals created by the PMT and test pulses, and measured pulse heights of the test pulse using HXD-AE'. Each test pulse from the random pulse generator was fed simultaneously to the CSA (with a $1 \mu\text{s}$ delay) and "PIN-trigger" input to HXD-AE', where the latter was used to acquire the former signal. This scheme was necessary to avoid large dead times if the CSA signals were used as self-trigger source. Under the presence and absence of the large LED signals, the pulse heights of the random test pulses were measured with HXD-AE', for various test-pulse voltages over 0–6 V. As a result, the pulse heights measured under the two conditions agreed with 1 % without any unexpected effects. Consequently, the effect of large signals cannot explain the change of the GSO energy scale.

Appendix 3. Calculation of Light Outputs from Activation Lines

A.3.1. Preparation for the Calculation

Here we show how to calculate light outputs for the 70, 150, 196 keV lines. We denote the light outputs of GSO to electron as $L_e(E)$, and the one to photon as L_γ .

To calculate the former, we adopted the approximation expression based on the experimental measurement of the light output to electron (Uchiyama et al. 2001),

$$L_e(E) = \left[1 - \frac{1.5}{E} \right] \times E. \quad (\text{A1})$$

Based on the ground measurement (Kitaguchi et al. 2005), the latter is described as

$$E = E_{\text{LO}}(E) [1 - \exp(-0.058 \times E_{\text{LO}}(E) - 0.53)].$$

$$L_\gamma(E) = \frac{(E_{\text{LO}}(E) - 8.1 \text{ keV})}{(E_{\text{LO}}(344 \text{ keV}) - 8.1 \text{ keV})} \times 344, \quad (\text{A2})$$

where E_{LO} is an intervening variable. The two functions, $L_e(E)/E$ and $L_\gamma(E)/E$ are plotted in figure 6. The binding energy, the fluorescence energies, and the fluorescence yields for several shells (K, L, M, ..) are denoted as $E_{K,L,M,..}$, $E_{K\alpha,..}$ and $f_{K,L,..}$, respectively. These parameters of ^{151}Eu are taken from the database of ENSDF³.

The light output caused by releasing the energy of the K(L, M, ..)-shell vacancy, after the electron bounded in K(L, M..) shell is ejected, should be calculated and defined as $LK(LL, LM, ..)$. There are two processes; the fluorescence X-ray emitted with the probability of $f_{K(L,M,..)}$, and the Auger electron emitted with the probability of $1 - f_{K(L,M,..)}$. Considering both effects, we can approximately express LK as

$$LK = f_K [L_\gamma(E_{K\alpha}) + L_e(E_K - E_{K\alpha})] + (1 - f_K)L_e(E_K), \quad (\text{A3})$$

and LL as

$$LL = f_L [L_\gamma(E_{L\alpha}) + L_e(E_L - E_{L\alpha})] + (1 - f_L)L_e(E_L). \quad (\text{A4})$$

In the case of M shell, we assume that all energies are released via the Auger electron, expressing LM as

$$LM = L_e(E_M). \quad (\text{A5})$$

Then, we define the light output from ejection of the

³ <http://www.nndc.bnl.gov/ensdf/>

electron from the K(L, M, ...) shell via the internal conversion, and denoted them as $L_{eK(eL,eM,...)}(E)$. It is written as

$$L_{eK,eL,eM,...}(E) = L_e(E - E_{K(L,M,...)}) + LK(LM,LL,...), \quad (A6)$$

where $E - E_{K(L,M,...)}$ represents the kinetic energy of the electron escaping from K(L, M, ...) -shell.

Finally, we define the light output via the gamma decay with the released energy of E as $L_O(E)$. $L_O(E)$ becomes a linear combination of $L_\gamma(E)$ and $L_{eK(eL,eM,...)}(E)$. Each weight of the sum is derived from the internal conversion coefficient for each shell, $\alpha(K, L, M, ...)$ (ref. ENSDF). Therefore, the expression of $L_O(E)$ is

$$L_O(E) = \frac{[L_\gamma(E) + \alpha(K)L_{eK}(E) + \alpha(L)L_{eL}(E) + \alpha(M)L_{eM}(E) + \dots]}{N}$$

where the N is the normalization factor and defined as

$$N \equiv 1 + \alpha(K) + \alpha(L) + \alpha(M) + \dots$$

In the following calculation, we considered the contribution from the electron and gamma emission inside the N-shell.

A.3.2. Results of the Light Outputs

We utilized the internal conversion coefficient of ^{151}Eu , because all the three lines are originated from the beta-decay of Gd. The light output of the 196 keV line is a sum of 174.70 keV and 21.53 keV, as described in Paper II. By using the notation defined in section A.3.1, this can be written as

$$L_\gamma(196.2 \text{ keV}) \longrightarrow L_O(174.7 \text{ keV}) + L_O(21.5 \text{ keV})$$

According to the equation (A7), we obtained $L_O(174.7\text{keV}) = 168.7$ and $L_O(21.5\text{keV}) = 18.3$, resulting in 186.9 by summing them, while $L_\gamma(196.2\text{keV}) = 192.7$. Therefore, the derived light output becomes lowered by 3.0%.

Likewise, the 150 keV line is the sum of the K-shell binding energy and the average energy of 43% from 103.2 keV and 39.2% from 97.4 keV, which are expressed as

$$L_\gamma(148.9 \text{ keV}) \longrightarrow \frac{[0.43L_O(103.2 \text{ keV}) + 0.40L_O(97.4 \text{ keV})]}{0.43 + 0.40} + LK.$$

We obtained $L_O(103.2 \text{ keV}) = 97.3$, $L_O(97.4 \text{ keV}) = 91.4$, and $LK = 42.3$, giving 136.8 in total, while $L_\gamma(148.9 \text{ keV}) = 144.3$. Thus, the light output from the 150 keV line becomes lowered by 5.2 %. The 70 keV line is the sum of the K shell energy and 21.5 keV, expressed by

$$L_\gamma(70 \text{ keV}) \longrightarrow L_O(21.5 \text{ keV}) + LK.$$

Considering $L_\gamma(70 \text{ keV}) = 64.2$, the light output from the 70 keV line becomes 60.5, lowered by 5.7 %.

References

- Fukazawa, Y., *et al.* 2006, SPIE
 Fukazawa, Y. et al. 2009, PASJ, 61, S17
 Jourdain, E., Roques, J. P., 2009, ApJ, 704, 17
 Kawaharada, M. 2002, Master thesis, Dept. of Physics, University of Tokyo

- Kawaharada, M., *et al.* 2004, Proc. SPIE, 5501, 286
 Kitaguchi, T., *et al.* 2006, SPIE, Vol. 6319
 Kokubun, M. *et al.* 1999, *IEEE Trans. Nucl. Sci.*, 46, 371
 Kokubun, M. *et al.* 1999, 59, 53-76
 Koyama, K. *et al.* 2007, PASJ, 59, 23-33
 Mitsuda, K. *et al.* 2007, PASJ, 59, 1-7
 Ozaki, M. *et al.* 2005, IEEE, Trans. Nucl. Sci, 53, 3, 1310-1316
 Serleimitsos, T. *et al.* 2006, PASJ, 59, 9-21
 Sulkimo, J. et al. 2003, Nuclear Instruments and Methods in Physics Research Section A, 506, 3, 1, 250-303
 Alison, J. et al. 2006, IEEE Transactions on Nuclear Science, 53, 1, 270-278
 Takahashi, T. *et al.* 2007, PASJ
 Tanihata, S. 1998, Master thesis, Dept. of Physics, University of Tokyo
 Terada, Y. *et al.* 2005, IEEE, Trans. Nucl. Sci, 52, 4, 902
 Terada, Y. *et al.* 2006, ApJL, 648, 139
 Terada, Y. *et al.* 2008, PASJ, 60, SP-1, 2008
 Terada, Y. *et al.* 2005, *IEEE Trans. Nucl. Sci.*, 52, 902
 Uchiyama, Y., *et al.* 2001, *IEEE Trans. Nucl. Sci.*, 48, 379
 Yamada, S. 2008, Master thesis, Dept. of Physics, University of Tokyo